
PERGAMON

Journal of Quantitative Spectroscopy & Radiative Transfer 71 (2001) 383–395

Journal of Quantitative Spectroscopy & Radiative Transfer

www.elsevier.com/locate/jqsrt

A Thomson scattering post-processor for the MEDUSA hydrocode

J. Hawreliak[a,*], D. Chambers[b], S. Glenzer[c], R.S. Marjoribanks[d], M. Notley[e], P. Pinto[b], O. Renner[f], P. Sondhauss[a], R. Steel[e], S. Topping[g], E. Wolfrum[a], P. Young[c], J.S. Wark[a]

[a] *Department of Physics, University of Oxford Parks Road, Oxford OX1 3PU, UK*
[b] *Steward Observatory, University of Arizona, Tucson, Arizona, AZ 85721, USA*
[c] *Lawrence Livermore National Laboratory, Livermore, CA 94550, USA*
[d] *Department of Physics, McLennan Physical Labs, University of Toronto, 60 St. George Street, Toronto, Ont., Canada M5S 1A7*
[e] *Rutherford Appleton Laboratory, Chilton, Didcot, Oxon. OX11 0QX, UK*
[f] *Institute of Physics, Czech Academy of Sciences, 18040 Prague, Czech Republic*
[g] *School of Mathematics and Physics, Queens University Belfast, Belfast BT7 1NN, UK*

Abstract

In order to understand the physical processes that occur in laser-produced plasmas it is necessary to diagnose the time-dependent hydrodynamic conditions. Thomson scattering is, in principle, an ideal diagnostic as it provides a non-intrusive method of measuring ion and electron temperature, electron density, plasma velocity, and heat flow. We describe here a post-processor for the MEDUSA hydrocode that simulates streak camera images of the Thomson spectra. The post-processor can be used in three ways: (1) creating simulated streak camera images that can be compared directly with experimental data, (2) evaluating experimental designs to determine the viability of the Thomson scattering diagnostic, and (3) as an automated data analysis routine for extracting hydrodynamic parameters from a calibrated experimental streak camera image.

Keywords: Thomson scattering; Laser-produced-plasma; Hydrocode

1. Introduction

Thomson scattering [1] is a powerful diagnostic of laser-produced plasmas (LPPs) because it can provide simultaneously a measurement of the electron density, electron and ion temperatures,

* Corresponding author.
E-mail address: j.hawreliak@physics.ox.ac.uk (J. Hawreliak).

0022-4073/01/$ - see front matter
PII: S0022-4073(01)00084-X

plasma expansion velocity, degree of ionisation and heat flow [2] in a non-intrusive manner. As such, one can obtain a vast wealth of time-dependent hydrodynamic data in a single image. It has been used successfully to diagnose the parameters in a wide range of plasmas, e.g., tokamaks [3], compact tori [4], Z-pinches [5], as well as LPPs [6,7].

In this paper we describe a Thomson scattering simulation tool which can be used in a variety of different modes to aid in the design and analysis of experiments where such scattering is used to probe the hydrodynamic conditions of a LPPs. The computer program can work both as a post-processor of a hydrodynamic simulation, and as a stand-alone tool to extract hydrodynamic parameters that are consistent with experimental streak camera data. In its present post-processor mode, the code uses input data from the widely used hydrodynamic code MEDUSA [8,9].

The paper is laid out in the following manner. We first present the fundamental theory of Thomson scattering. Whilst this is well known, we present the theory here to make explicit the assumptions currently incorporated within the program, especially as regards the modelling of heat flow and the spectral range over which the routines have thus far been used to extract experimental data. Secondly we present simulated time-resolved Thomson scattering spectra produced by using the code to post-process MEDUSA output for a planar freely ablating LPP. Finally, we demonstrate the determination of time-dependent hydrodynamic conditions from an experimental streak-camera image of scattered radiation centred around the ion acoustic feature.

2. Theory of Thomson scattering

2.1. Collective versus non-collective scattering

The spectra of Thomson scattered radiation depends upon the scattering parameter, α, which determines whether the scattering is sensitive to the plasma wave fluctuations.

$$\alpha = \frac{1}{k\lambda_D}, \tag{1}$$

where k is the scattering wave vector, $k = k_s - k_0$ where k_s is the scattered wave vector and k_0 is the probe wave vector as defined below in Fig. 1 and λ_D is the Debye length of the electrons.

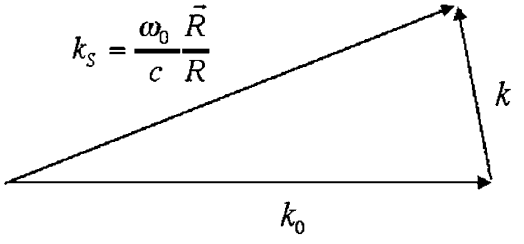

Fig. 1. The scattering in the plasma, k_0 probe wave vector, k_s scattered wave for probe frequency, ω_0, and collector direction **R** and k is the scattering wave vector which in the collective regime corresponds to plasma wave fluctuation.

When the probe wavelength is small compared with the Debye length, $\alpha < 1$, and the scattering occurs from individual electrons. The plasma effects have to be taken into consideration for longer probe wavelengths where collective effects are important, i.e. when $\alpha > 1$. For large values of α, there is a resonance in the amplitude of the scattered radiation, corresponding to the scattering of the radiation from distinct plasma wave fluctuations, as shown schematically in Fig. 1.

2.2. Scattering cross section

A detailed calculation can be performed following the technique given by Evans and Katsenstein [10] for the scattering cross section.

$$\sigma(\mathbf{k},\omega) = \sigma_T S(\mathbf{k},\omega), \tag{2}$$

$$S(\mathbf{k},\omega) = \left| \frac{1 - G_i(\omega/k)}{1 - G_e(\omega/k) - G_i(\omega/k)} \right|^2 f_{0e}(\omega/k) + Z \left| \frac{G_e(\omega/k)}{1 - G_e(\omega/k) - G_i(\omega/k)} \right|^2 f_{0i}(\omega/k), \tag{3}$$

$$G_e = -\alpha^2 W(x_e), \tag{4}$$

$$G_i = -Z \frac{T_e}{T_i} \alpha^2 W(x_i), \tag{5}$$

$$W(x) = 1 - 2x e^{-x^2} \int_0^x e^{p^2} \, dp - i\pi^{1/2} x e^{-x^2}, \tag{6}$$

where $\sigma_T = (8\pi r_e^2/3) \sin^2 \beta$ is the Thomson scattering cross section of a free electron with classical radius r_e, β the angle between the polarisation of the probe radiation and the direction of collected radiation, and $S(\mathbf{k},\omega)$ is the dynamic structure factor for scattering vector k and frequency shift ω. Z is the ionic charge, and T_e and T_i are the electron and ion temperatures, respectively. For a plasma with Maxwellian distribution functions, f_0, of both electrons and ions, the functions G_e and G_i are given by Eqs. (4) and (5), respectively.

For large values of α we note that a resonance occurs in the intensity of the scattered radiation at the Bohm–Gross frequency:

$$\omega_{bg}^2 = \omega_p^2 + \left(\frac{3k_B T_e}{m_e} \right) k^2, \tag{7}$$

where the plasma frequency is given by $\omega_p = (n_0 e^2/\varepsilon_0 m_e)^{1/2}$.

Similarly, for large values of $ZT_e\alpha^2/T_i$ a resonance occurs at the ion acoustic frequency

$$\omega_{ia}^2 = \frac{T_e}{m_i} \left(\frac{Z}{1 + k^2 \lambda_D^2} + \Gamma_i \frac{T_i}{T_e} \right) k^2 \approx \left[\frac{T_e}{m_i} \left(\frac{Z}{1 + k^2 \lambda_D^2} \right) \right] k^2, \tag{8}$$

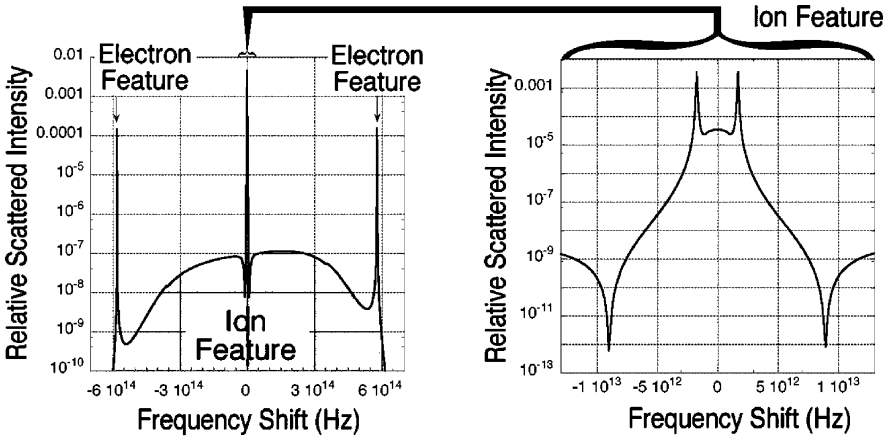

Fig. 2. The Thomson scattering spectrum scattered from a Maxwellian plasma with parameters as given in the text.

where Γ_i is the ratio of the specific heats. These resonances manifest themselves in the scattered spectra at $\pm\omega_{bg}$ and $\pm\omega_{ia}$ from the frequency of the input probe beam, ω_0. In general, it is the observation of the scattered spectrum in the vicinity of these resonances that yield information concerning the conditions within the plasma. As an example we show in Fig. 2 a simulated scattered spectra for radiation of wavelength 263.3 nm scattering through 90° from a plasma with an electron density of $3 \times 10^{26}\,\mathrm{m}^{-3}$, electron temperature of 2000 eV, and ion temperature of 1000 eV.

2.3. Modelling heat flow

In our modeling of the scattered radiation we assume that the distribution functions of both electrons and ions are Maxwellian. However, the laser energy deposited at the critical surface flows down the temperature gradient to the denser, cooler surface resulting in the ablation of material with corresponding mass flow. Clearly such a process involves non-Maxwellian distribution functions of the electrons. Within the framework described here, we assume that such heat flow does not significantly perturb the shape of the distribution function, and that its main influence is to shift the distribution function of the electrons with respect to that of the ions. It is well known that a relative drift velocity between the electrons and ions results in an asymmetry of the intensity of the two ion acoustic peaks [10] and thus such asymmetry can be used as a diagnostic of the degree of heat flow [2].

We assume that the electron distribution function that incorporates the heat flow is given by a Maxwellian with a shifted velocity U:

$$f_e = \frac{n}{v_e \pi^{1/2}} \exp\left[-\left(\frac{v-U}{v_e}\right)^2\right]. \tag{9}$$

Note that the peak of the distribution function is shifted to a velocity that is opposite in direction to that of the heat flow, as quasi-neutrality requires no net current. The bulk of the heat flow occurs due to relatively fast electrons, as heat flow is proportional to the integral of

the distribution function multiplied by v^3, and to offset this a cold return current must flow in the opposite direction. Clearly the scattering will be dominated by the majority of the electrons, which are represented by this return current. Within this simple approximation the shift in the Maxwellian is related to the heat flow, Q [11]. Thus,

$$U = -\frac{9\pi}{640}\left(\frac{\gamma_T}{\gamma_E \delta_T \varepsilon_C}\right)\frac{Q}{n_e T_e} \tag{10}$$

where γ_T, γ_E, δ_T and ε_C are coefficients depending on Z, for aluminium $\gamma_T/(\gamma_E\delta_T\varepsilon_C) \approx 3.1$. Care should be taken when simulating heat flow in this manner, as clearly the approximation will not be valid in regimes of large heat flux when the distribution function can be greatly distorted [12,13].

Given the relation between heat flow and effective drift velocity between the electrons and ions, we can follow the analysis of Evans and Katsenstein once more [10]. They demonstrate that the Thomson spectrum for a plasma where the electrons have a relative velocity to the ions of U_k is given by replacing

$$x_e \Rightarrow x_e - y, \tag{11}$$

$$y = \frac{U_k}{v_e} \tag{12}$$

in Eqs. (3)–(6).

3. The post-processor

The post-processor solves the scattering equations to provide an absolute wavelength and direction dependent scattered intensity for a given electron and ion density, mean ionisation, electron and ion temperature, and heat flow. In the post-processor the time- and space-dependent quantities are provided by the MEDUSA hydrocode [8,9].

In any experimental set-up we collect radiation scattered from a particular volume in space that is defined by the beam profile of the input scattering beam, and by the subsequent collecting optics. A schematic of a typical experimental set-up is shown in Fig. 3. In this case the collecting system is set-up along the axis of the plasma expansion so that it can measure the Doppler shift in the spectrum to get a measure of the plasma velocity.

MEDUSA is a Lagrangian code, and thus for every time step for which the spectrum is to be calculated the post-processor first determines which Lagrangian cells lie within this volume of interest. Then, for each of these Lagrangian cells, the scattered intensity is weighted by a function that takes into account the intensity distribution of the input beam (at present assumed to be Gaussian) and the efficiency of the collecting optics as a function of space. The Thomson spectrum from each cell is then shifted in frequency to take into account the motional Doppler shift.

An experimental collecting system images the scattered probe beam onto the slit of a spectrometer. The post-processor takes into account the efficiency and finite spectral resolution of the spectrometer by appropriate convolution with the instrument response functions. Similarly, if the spectra is time-resolved with a streak camera, the finite temporal resolution of the streak-camera

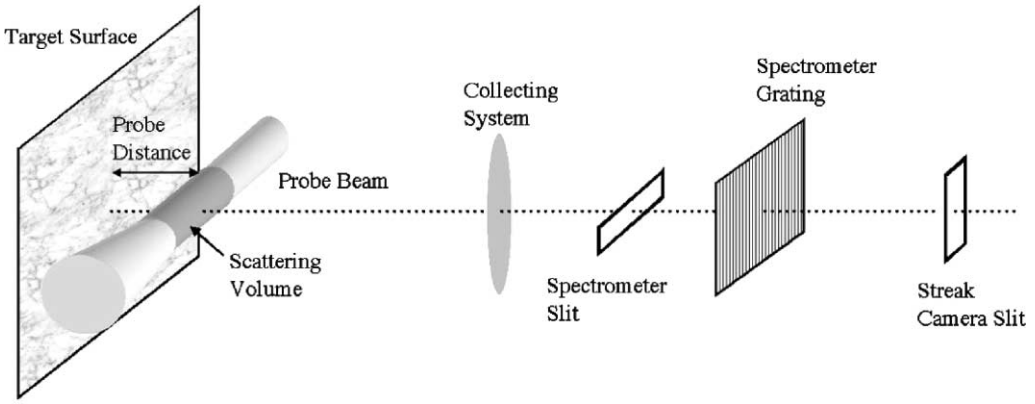

Fig. 3. Schematic diagram of a typical experimental set-up to obtain a time resolved Thomson scattered spectrum.

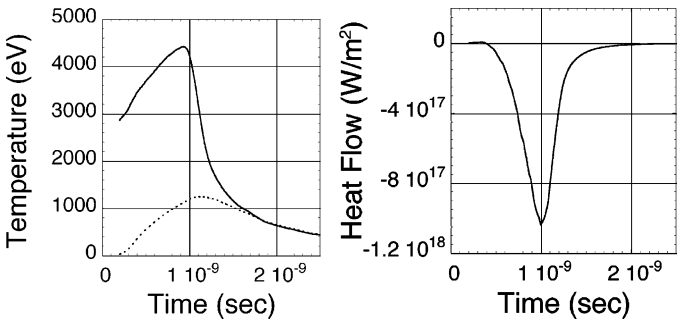

Fig. 4. Electron temperature, solid line, ion temperature, dashed line, and heat flow from MEDUSA as a function of time.

can also be taken into account by convolving the predicted time-dependent spectrum with the instrument function of the streak camera.

3.1. Post-processor output

To illustrate the post-processor we will diagnose a MEDUSA simulation. We simulate the hydrodynamic evolution of a 12 μm thick Al foil target irradiated by a 1 kJ, 1053 nm, 1 ns laser pulse (100 ps rise and fall) within a 500 μm diameter focal spot. This corresponds to peak intensities of $5 \times 10^{14}\,\mathrm{W/cm^2}$, and is similar to those used in experiments to be described in Section 4.1.

In the post-processor the Thomson probe beam is perpendicular to the plasma expansion at 300 μm in front of the original target surface. The probe beam is taken to be Gaussian with a FWHM of 20 μm and a wavelength of 263.3 nm. The radiation is assumed to be collected with an $f/10$ collecting system along the direction of plasma flow, i.e., normal to the target surface.

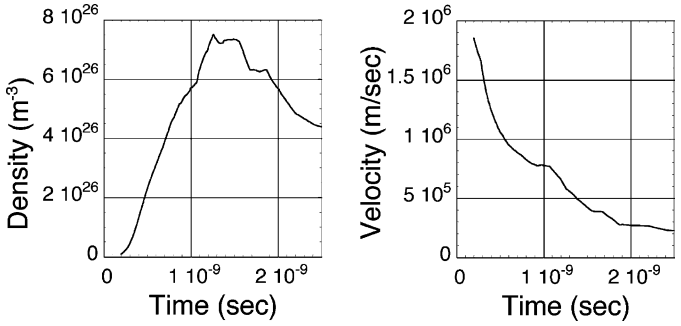

Fig. 5. Density and plasma velocity as a function of time.

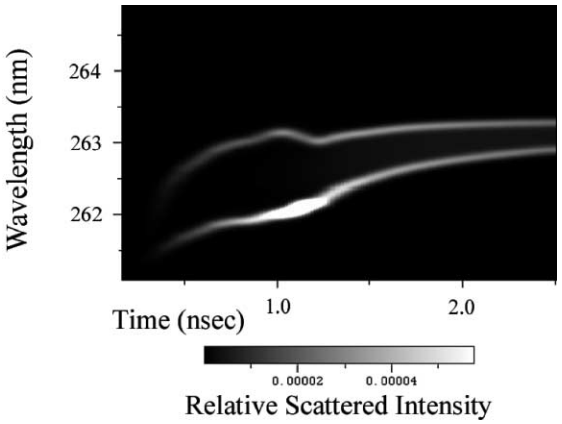

Fig. 6. Simulated Thomson scattering streak image.

In Figs. 4 and 5 we show the time-dependent hydrodynamic variables predicted by MEDUSA at the position of the centre of the probe beam 300 μm in front of the initial surface of the target.

The corresponding simulated time-dependent Thomson scattering image from the post-processor is shown in Fig. 6 for the wavelength range that encompasses the ion acoustic resonances. There are several features to note. Firstly, we see that the central frequency of the scattered radiation is shifted due to the motional Doppler effect, and that this velocity falls as a function of time, consistent with the hydrodynamic simulations. Furthermore, the separation between the two ion acoustic peaks reduces as time proceeds. This separation is related to the electron temperature, as shown in Eq. (8). Furthermore, the ion acoustic features are clearly asymmetric in their intensity at early times, consistent with the large values of the heat flow at these times. Finally, the frequency integrated intensity of the scattered radiation rises and falls in a manner consistent with the history of the electron density. [1] Note that within this simulation

[1] For this analysis we have assumed a constant intensity probe beam though the temporal shape of the probe beam can easily be taken into account.

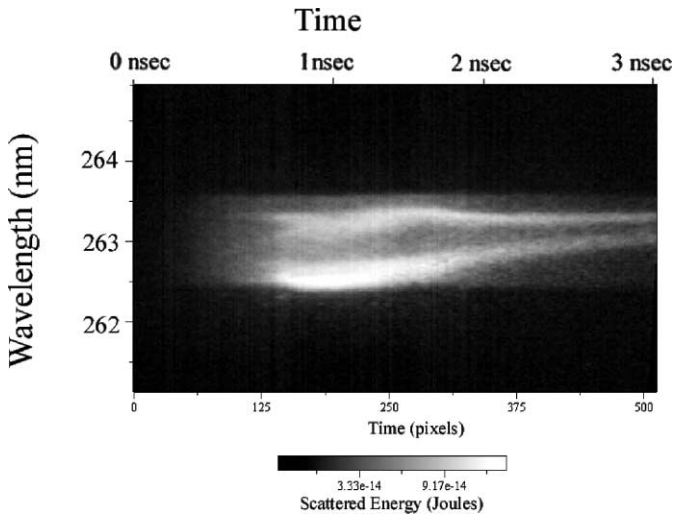

Fig. 7. An experimental time-resolved Thomson scattering image after it has been calibrated in wavelength and time, see text for details.

the combined spectral resolution of the spectrometer and streak camera is 30 nm which is the resolution observed the experiment described in Section 4.1.

4. Data analysis

As well as using the Thomson scattering code to post-process hydrodynamic data, we have also developed a data analysis routine that takes calibrated experimental Thomson spectra, and automatically finds the electron and ion temperatures, electron density, velocity, and heat flow that are consistent with the data. This computer program is particularly useful when applied to a time-dependent spectrum recorded on a streak camera, as it then predicts these variables as a function of time. In its present form, the routine analyses only the ion feature to deduce the variables. However, the routine can also be adapted to find the best fit to the electron feature.

The routine takes as its input an experimental streak camera image of the ion acoustic feature with the temporal and spectral axes, as well as an absolute intensity scale defined. This calibration is provided in the form of an input file containing the upper and lower wavelength limits of the image, the time per pixel, and the energy necessary to register one count for a given pixel. The input file also includes information about the experimental geometry, such as the scattering and collection angles.

A calibrated image in TIFF format, see Fig. 7, is read and fills a matrix whose indices correspond to time and wavelength divisions. The routine then takes each time step in turn, determining the hydrodynamic parameters consistent with the data at each time step.

The hydrodynamic parameters consistent with the data are found by an iterative method that relies heavily on knowledge of the separation in wavelength between the two ion acoustic peaks. That is, the experimental data is used to provide initial estimates of V, n_e, T_e, T_i,

and the heat flow, Q, as described by Eq. (10). At present the code requires as input of the degree of ionisation, Z. Given these hydrodynamic variables, a simulated Thomson spectra is generated, and compared with experiment. The differences between the location and asymmetry of the experimental and simulated ion acoustic peaks are then used to provide revised estimates for the hydrodynamic variables, V', T'_e, T'_i, and the heat flow, Q'. Iteration proceeds until the simulated location and asymmetries of the ion acoustic peaks agree with those present in the data within user specified limits.

The initial guess of the electron density is provided in an input file rather than taken from the data. The condition of $\alpha > 1$ puts limits on values that can be used for the initial electron density guess. For example, in experiments where the probe wavelength is 263.3 nm, as described below, we estimate n_e to be $1 \times 10^{26}\,\mathrm{m}^{-3}$. As explained below, rapid iteration to a stable value of the electron density occurs by comparison between the computed and absolute scattered intensities.

The wavelengths of the two ion acoustic peaks is automatically determined by the code using a maxima location routine. The locations of the peaks are labelled as λ_1 and λ_2 for the shorter and longer wavelength peak, respectively. The wavelengths at which the two peaks occur are symmetric about the probe wavelength in the reference frame of the plasma, and thus the plasma expansion velocity is immediately determined. For a planar expansion with the probe beam normal to the target and the collecting system parallel to the direction of plasma expansion, the velocity of the expansion is calculated from Eq. (13).

$$V = c\left(1 - \frac{\lambda_c}{\lambda_0}\right), \qquad \lambda_c = \frac{\lambda_1 + \lambda_2}{2}, \tag{13}$$

where V is the plasma expansion velocity, λ_0 is the wavelength of the probe beam and λ_c central wavelength between the two peaks.

Once the plasma velocity has been determined from the mean wavelength of the ion acoustic features, the routine then uses the separation between the features to estimate the electron temperature. That is, using Eq. (8) we have for the initial estimate

$$T_e = \frac{m_i}{Z}\left[\frac{2\pi c \Delta\lambda}{\lambda_0(\lambda_0 + \Delta\lambda)}\right]^2, \qquad \Delta\lambda = \left|\frac{\lambda_2 - \lambda_1}{2}\right|. \tag{14}$$

At this stage we have no information concerning the value of the ion temperature, and thus it is initially set equal to the electron temperature.

An initial estimate of the heat flow is based on the degree of asymmetry in the ion acoustic peaks. We first define an asymmetry factor, θ defined as

$$\theta = \frac{s(\lambda_2) - s(\lambda_1)}{\max(s(\lambda_2), s(\lambda_1))},$$

where $s(\lambda)$ is the intensity at λ. The estimate of the heat flow is then given by

$$Q = 5.79 \times 10^{-2} v_e^3 n_e m_e \theta, \tag{15}$$

where v_e is the electron thermal velocity, n_e is the electron density and m_e is the electron mass.

These initial estimates for the plasma hydrodynamic parameters are used to simulate a Thomson scattered spectrum. The simulated spectrum is convolved with a Gaussian instrument function obtained from the width of the ion features. The plasma parameters for the next iteration are found in the following manner:

- $V' = V$, (the velocity of the plasma is only determined by the central wavelength of the ion acoustic feature, and is thus completely determined by the data and initial calculations.)
- n_e' is calculated by scaling the integrated intensity of the simulated scattered spectrum to match that of the measured spectrum knowing the intensity of the probe beam.
- T_e' is determined from the wavelength separation of the ion acoustic peaks in the simulated spectrum, $\Delta\lambda_s$. The new value of the electron temperature is then given by

$$T_e' = \frac{\Delta\lambda}{\Delta\lambda_s} T_e. \tag{16}$$

- T_i' is found by using the full form of the ion acoustic dispersion from Eq. (14):

$$T_i' = m_i \left(\frac{1}{k_s^2} \left[\frac{2\pi c \Delta\lambda}{\lambda(\lambda + \Delta\lambda)} \right]^2 - \frac{T_e Z / m_i}{1 + (k_s^2 \lambda_D^2)} \right), \tag{17}$$

  where the new values, n_e', and T_e' are used to determine the Debye length.
- Q' is determined from the previous estimate, Q, by scaling using Eq. (18),

$$Q' = \frac{Q^*}{Q_s} Q, \tag{18}$$

  where Q^* is calculated using Eq. (15) with θ determined from the data and the updated values of density, n_e', and temperature, T_e'. Q_s is calculated using Eq. (15) with n_e', T_e' but with θ_s extracted from the simulated spectrum. In this way the iteration proceeds until the measured asymmetry, θ, and the simulated value, θ_s, agree to within the user defined limit.

The new values are used to generate the next simulated spectrum for comparison with the experimental spectrum, and iteration proceeds for each time step until $(|\Delta\lambda_s - \Delta\lambda|)$ and $(|\theta_s - \theta|)$ are within some predetermined limits set by the user.

4.1. Experimental data analysis

As an example of the use of this routine, we show in Fig. 7 a streak camera image of the Thomson spectrum from a Al foil target irradiated by approximately 1 kJ of 1053 nm laser energy in 1 ns at the Vulcan laser facility at the Rutherford Appleton Laboratory. A 263.3 nm probe beam was focused to a 50 μm spot 300 μm in front of the target surface collected into a f/10 collecting system, spectrally resolved by a 1 m spectrometer using a 3600 l/mm grating and temporally resolved with a Imacon 500 UV streak camera.

The hydrodynamic variables consistent with this experimental data were computed. The simulated Thomson spectrum which provided the best fit to the data is shown for comparison in

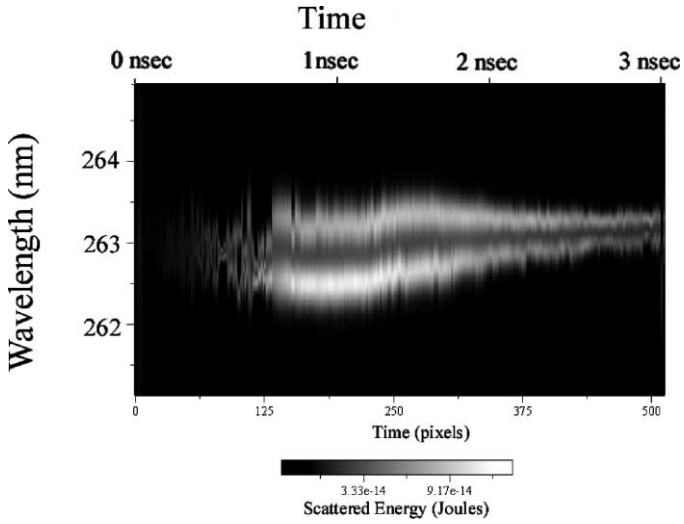

Fig. 8. The simulated time-dependent Thomson spectrum to be compared with Fig. 7.

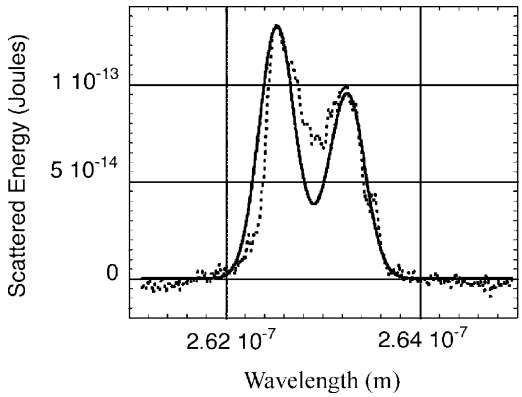

Fig. 9. A trace at $t = 1$ ns, the solid line is a trace from the simulated spectrum, Fig. 8, and the dashed line is from the experimental data, Fig. 7.

Fig. 8. Fig. 9 is a trace taken from the data and the fit at 1 ns to show the quality of the analysis. Excellent overall agreement can be seen. The hydrodynamic parameters extracted from the analysis are shown in Figs. 10 and 11.

5. Conclusion

In summary, we have developed a Thomson scattering post-processor that can be used in three ways: (1) simulation for comparing simulation directly to data from experiment, (2) evaluating experimental designs where Thomson scattering will be used as a diagnostic, and (3)

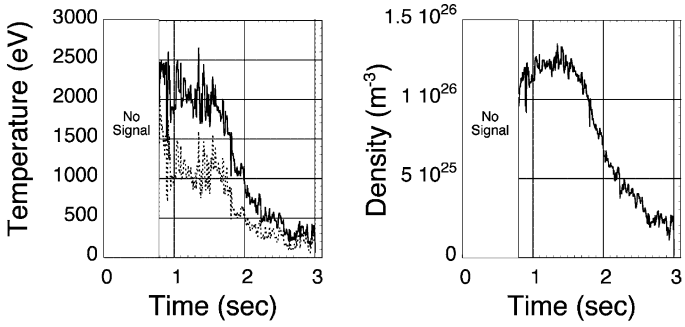

Fig. 10. Electron temperature, solid line, ion temperature, dashed line, and density for the simulated fit to the experimental streak image.

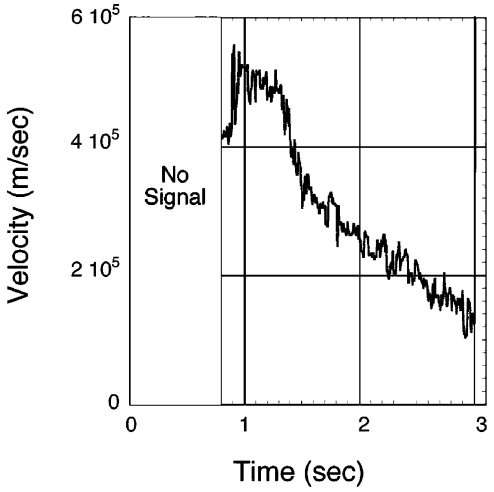

Fig. 11. Velocity for the simulated fit to the experimental streak image.

an automated data analysis routine that can extract hydrodynamic parameters from calibrated images. From input files created by the hydrodynamic code MEDUSA the post-processor is successful in generating images in the ion-acoustic feature wavelength range that are consistent with experimental data. The data analysis routine has been shown to be capable of extracting hydrodynamic parameters recreating a spectrum that fits the data well. Future work will concentrate on using the post-processor for detailed analysis of experimental spectra.

Acknowledgements

The authors are grateful for the support from the staff of the Central Laser Facility at the Rutherford Appleton Laboratory. This work was supported by grants from the Engineering and Physical Sciences Research Council and the Department of Energy.

References

[1] Kunze HJ. In: Lochte-Holtgreven W, editor. Plasma diagnostics. Amsterdam: North-Holland, 1968, p. 550.
[2] Cameron SM, Camacho JF. J Fusion Energy 1995;14:373.
[3] Allen SL, Hill DN, Carlstrom TN, Nilson DG, Stockdale R, Hsieh CL, Petrie TW, Leonard AW, Ryutov D, Porter GD, Maingi R, Wade MR, Cohen R, Nevins W, Fenstermacher ME, Wood RD, Lansnier CJ, West WP, Brown MD. J Nucl Mater 1997;241–243:595.
[4] Coomer E, Hartman CW, Morse E, Reisman D. Nucl Fusion 2000;40:1669.
[5] Gray DR, Kilkenny JD. Plasma Phys 1980;22:81.
[6] Glenzer SH, Rozmus W, MacGowan BJ, Estabrook KG, De Groot JD, Zimmerman GB, Baldis HA, Harte JA, Lee RW, Williams EA, Wilson BG. Phys Rev Lett 1999;82:97.
[7] Glenzer SH, Alley WE, Estabrook KG, De Groot JS, Haines MG, Hammer JH, Jadaud JP, MacGowan BJ, Moody JD, Rozmus W, Suter LJ, Weiland TL, Williams EA. Phys Plasmas 1999;6:2117.
[8] Christiansen JP. Comput Phys Commun 1974;7:271.
[9] Djaoui A, Rose SJ. J Phys B 1992;25:2745.
[10] Evans DE, Katsenstein J. Rep Prog Phys 1969;32:207.
[11] Monchicourt P, Holstein PA. Phys Fluids 1980;23:1475.
[12] Bychenkov VYu, Myatt J, Rozmus W, Tikhonchuk VT. Phys Plasmas 1994;8:2419.
[13] Dragila R. J Appl Phys 1985;58:4539.